J. Fluid Mech. (1989), *vol.* 200, *pp.* 217–233
Printed in Great Britain

The instability of a liquid film on a wall exposed to an air flow

By H. LUDWIEG† AND H. HORNUNG‡

†DFVLR Institute for Experimental Fluid Mechanics, D-3400 Göttingen, Bunsenstr. 10, FRG

‡Graduate Aeronautical Laboratories, California Institute of Technology, Pasadena, CA 91125, USA

(Received 16 June 1987 and in revised form 18 August 1988)

The title problem, which is an important early element of the mechanism of the development of a surface oil flow visualization picture, is studied by a linear stability analysis that predicts the most strongly amplified wavenumber of transverse surface waves as a function of Reynolds number, surface tension, film viscosity and initial thickness of the film. Wall scaling virtually removes the additional dependence on Reynolds number. In a simple experiment the observed wavenumber agrees with the predicted most strongly amplified value to within the experimental accuracy.

1. Introduction and aim

One of the most effective tools in aerodynamics research and development is the method known as surface oil flow visualization. In this technique, a thin film of a suspension of finely ground solid particles in a liquid is sprayed onto the model, the flow around which is to be investigated. The model is then exposed to the flow in a wind tunnel until the suspension flows under the influence of the forces exerted on it by the air. Depending on the liquid chosen, the film may eventually dry out, leaving the particles behind. During the time in which the film flows, the particles arrange themselves in lines which are usually interpreted as being aligned with the shear stress that would be exerted on the model in the absence of the film (see e.g. L. C. Squire 1961). The method thus supplies a very valuable and immediate picture, which transmits the considerable wealth of data contained in the direction field of the wall shear stress to the best pattern-recognition device, the human eye.

An example of such a pattern is shown in figure 1. As can be seen, the pattern is not only structured in lines, but other features, such as the density, granularity and contrast of the lines, also vary within the pattern. Clearly, any liquid particle travels over a considerable fraction of the model length, so that local features of the pattern may well depend significantly on the conditions it has undergone on the way. Nevertheless, it is conceivable that local features correlate sufficiently well with quantities of interest (such as the magnitude of the wall shear stress) to provide an approximate measure of their local value. Hence there exists a practical motivation for an understanding of the mechanism of the formation of the pattern.

There is no *a priori* reason to expect line formation at all. Its mechanism is therefore an interesting fluid mechanical problem in itself, arising from some instability of the interaction between the air and liquid flows. In order to study it, this paper considers a model problem, in which not a suspension, but a pure liquid is taken to wet a flat plate. From a preliminary investigation (Hornung 1985) it became clear that the surface tension of the liquid plays a significant role in an early

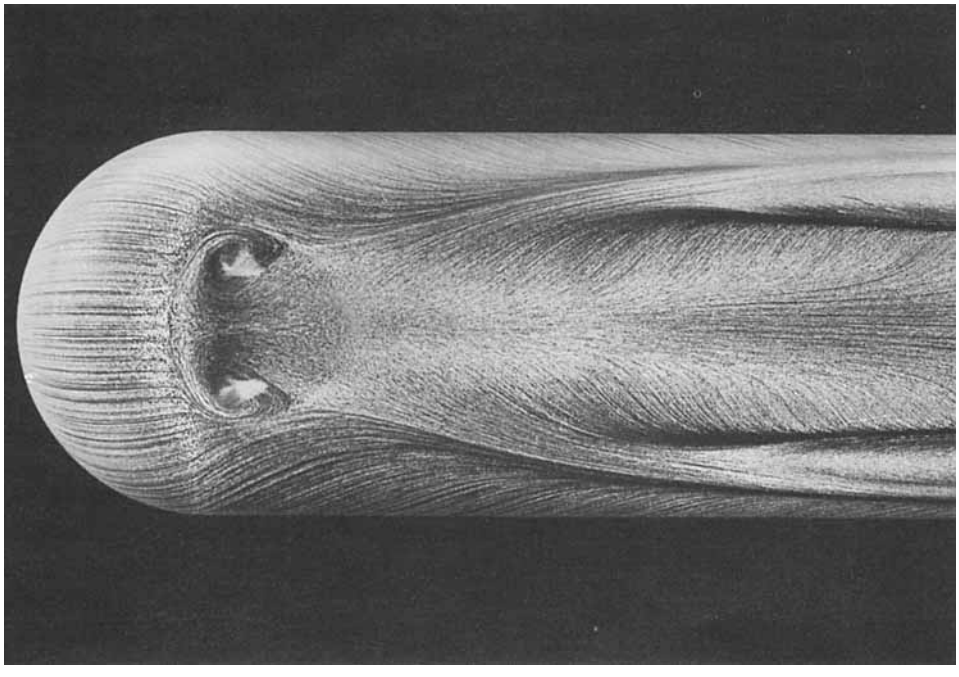

FIGURE 1. Example of an oil flow visualization photograph. Separation pattern (owl face of the second kind) on the lee side of a hemisphere cylinder at incidence. (Photograph provided by H. Bippes 1985).

stage of the mechanism, droplets being formed on the surface with a density that increases with τ/σ, where τ is the wall shear stress and σ is the surface tension between the liquid and the air. In the expectation that the instability of the liquid–air interface is the important element in the first stage of line formation, our aim is to determine the existence and features of this instability theoretically and experimentally.

The formation of lines clearly involves more complex three-dimensional and nonlinear processes than can be accounted for by the two-dimensional linear stability analysis presented here. We must emphasize that the problem tackled here, while being motivated by the line formation problem, accounts only for the initial stage of the formation of transverse waves.

Of the previous work on this subject, that of Craik (1966) is the most important. Craik considered the transverse waves generated in a liquid film wetting one wall of a turbulent channel flow of air. He determined the stability boundaries of the film surface in a theoretical analysis and compared these with his experiments on relatively thick films in the context of the oil flow visualization case. The mechanism of the instability observed by Craik was that the pressure in phase with the wave elevation and the tangential stress in phase with the wave slope act to destabilize the wave while surface tension and gravity stabilize it. The mechanism is the same in our case, with the exception that we consider much thinner films in which gravity plays no part. As has been observed by Craik, such thin films are unstable at all air-stream speeds. In the current paper we accordingly address the most strongly amplified wavenumber rather than the stability boundaries. Because the dimensionless parameters of our problem are considerably different from those of Craik, it is

necessary to relax some of the assumptions made by him. For example, the assumption that the streamwise derivatives may be neglected relative to the wall-normal derivatives is not justifiable for the short wavelengths that occur in our problem.

In order to compare the predicted most strongly amplified wavenumber with experiment, it is necessary to set up an experiment in which the flow is impulsively started and to observe the temporal development of the waves. The main interest here is in the flow over a flat plate with a laminar air boundary layer.

H. B. Squire (1953) also investigated a related phenomenon, the antisymmetric transverse waves that grow on a thin liquid sheet flowing into still air. While our analysis follows very similar lines to that of Squire, the results are considerably different because of the different boundary conditions. In particular, the wavenumbers of the antisymmetric waves predicted by Squire, which are in good agreement with experiment, are much smaller than those observed in wall flows.

2. Theory

2.1. *Problem definition and method of solution*

We shall examine whether the flow occurring in surface oil flow visualization, i.e. that of the liquid film and the air, can become unstable in such a manner that shallow, wave-like disturbances of the liquid surface grow with time. The dependence of the amplification of these waves on the wavelength and thus the most strongly amplified wavelength will be determined. Waves that have approximately this wavelength should be observable.

A wave-like disturbance of the liquid surface is assumed to be present. Since the motion of the liquid is very slow compared with that of the air, the air flow is virtually stationary and may be calculated by considering this wave-like disturbance as being rigid and at rest. In a second step the liquid flow is calculated. The external forces driving the liquid flow are the pressure and shear-stress distributions obtained in the air flow calculations and the surface tension between the liquid and air. The solution of this problem yields the amplification or damping of the assumed wave and its wavespeed.

We first apply this method to laminar air boundary layers and then give an approximate result for turbulent boundary layers. The flow is assumed to be two-dimensional throughout.

2.2. *Calculation of the air flow*

Consider a wall that is covered with a layer of liquid of constant thickness h. The air flows over this film with a laminar boundary layer of thickness δ. We neglect the unusually small streamwise gradients of undisturbed velocity outside the boundary layer, of the boundary-layer thickness and of its velocity profile.

The assumed initial disturbance is shown in figure 2. The amplitude s of this wave is assumed to be small compared with h and with the wavelength. The x-axis of the rectangular coordinate system is chosen to coincide with the undisturbed liquid surface.

We seek solutions in which the stream function ψ of the disturbance flow caused by the waviness of the wall takes the form

$$\psi(x, y) = \phi(y)\, \mathrm{e}^{\mathrm{i}\alpha x}. \tag{1}$$

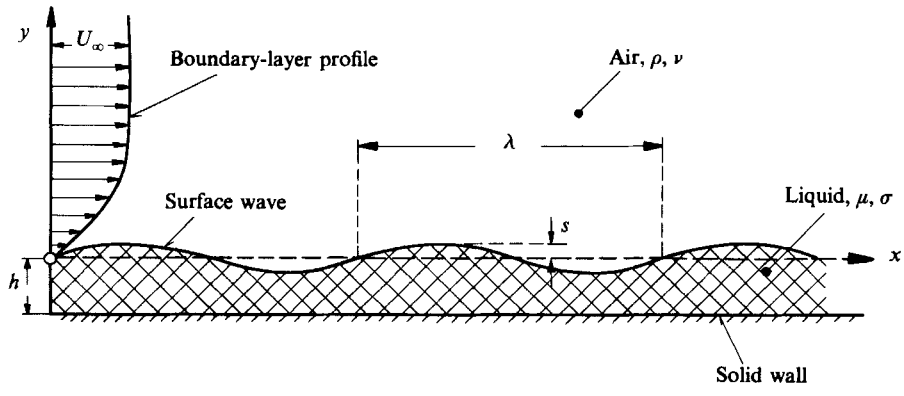

FIGURE 2. Defining sketch.

Linearizing the Navier–Stokes equations and eliminating the pressure, we obtain the following differential equation for ϕ:

$$U\phi''-\alpha^2U\phi-U''\phi=-\frac{\mathrm{i}\nu}{\alpha}(\alpha^4\phi-2\alpha^2\phi''+\phi''''), \tag{2}$$

where $U(y)$ is the velocity profile of the undisturbed boundary layer, α is the disturbance wavenumber $(2/\pi\lambda)$, ν is the kinematic viscosity of the air and the prime denotes differentiation with respect to the independent variable. Equation (2) is the well-known Orr–Sommerfeld equation for the case where the wave velocity is zero. Note, however, that the origin of the y-coordinate is at the mean position of the liquid–air interface, so that the boundary conditions must be correspondingly formulated.

We introduce the dimensionless variables

$$\left.\begin{aligned}\eta=\frac{y}{\delta},\quad \xi=\alpha x,\quad g(\eta)=\frac{U}{U_\infty},\\ A(\eta)+\mathrm{i}B(\eta)=\frac{\phi}{U_\infty s},\quad Re=\frac{U_\infty\delta}{\nu},\quad \alpha_*=\alpha\delta.\end{aligned}\right\} \tag{3}$$

Substituting these in (2) and separating real and imaginary parts we obtain the following coupled pair of fourth-order differential equations for the functions A and B:

$$\left.\begin{aligned}-gB''+g''B+\alpha_*^2gB=(\alpha_*Re)^{-1}(\alpha_*^4A-2\alpha_*^2A''+A''''),\\ gA''-g''A-\alpha_*^2gA=(\alpha_*Re)^{-1}(\alpha_*^4B-2\alpha_*^2B''+B'''').\end{aligned}\right\} \tag{4}$$

The boundary conditions require that the x- and y-components of the velocity (u and v) vanish at the liquid surface and that the disturbance velocity approaches zero as $\eta\to\infty$.

Let the value of η at the liquid–air interface be given by

$$\eta_\mathrm{w}=(s/\delta)\,\mathrm{e}^{\mathrm{i}\xi}, \tag{5}$$

so that, in the linearized approximation, the following boundary conditions result at $\eta=0$:

$$\left.\begin{aligned}A(0)=0,\quad B(0)=0,\\ A'(0)=-g'(0),\quad B'(0)=0.\end{aligned}\right\} \tag{6}$$

The finite value of $A'(0)$ results from the fact that the velocity profile of the undisturbed flow would have a finite x-component at the liquid surface. This has to be compensated by the disturbance flow. In the linearized approximation this compensation can be achieved by specifying the appropriate condition not at the liquid surface but at $\eta = 0$.

The boundary condition at $\eta = 1$ is obtained as follows. For $\eta > 1$, $g = 1$, and (4) then have inviscid solutions of the form $e^{(\alpha_* \eta)}$ and $e^{(-\alpha_* \eta)}$. Only the second provides the desired asymptotic behaviour as $\eta \to \infty$. The viscous solution can be omitted as usual. Therefore the following boundary conditions must be satisfied:

$$\left.\begin{aligned} A'(1) &= -\alpha_* A(1), \quad B'(1) = -\alpha_* B(1), \\ A''(1) &= -\alpha_* A'(1), \quad B''(1) = -\alpha_* B'(1). \end{aligned}\right\} \tag{7}$$

Equations (6) and (7) provide eight boundary conditions for the two linear fourth-order differential equations (4). By solving these numerically we obtain the desired disturbance flow, in the linear approximation. In particular,

$$A''(0) + iB''(0)$$

gives the additional shear stress caused by the waviness of the liquid–air interface, and

$$A'''(0) + iB'''(0)$$

gives the additional x-component of the pressure gradient. For the calculation of the liquid flow, only these two quantities are required from the air flow calculation. Since they are complex, both the shear stress and the pressure gradient are phase-shifted relative to the liquid surface.

2.3. *Calculation of the liquid flow*

We now consider the liquid flow, where the (Newtonian) liquid covers the wall with uniform thickness h, modulated by a differentially small waviness as in the previous section. The following external forces act on the liquid: the constant shear stress of the undisturbed air boundary-layer flow; the shear-stress and pressure-gradient forces exerted by the air as calculated by the procedure of the previous section; and the surface-tension forces which occur because of the curvature of the liquid surface and can be considered in the form of an additional pressure applied at the surface.

For a sufficiently viscous liquid and sufficiently small film thickness, both the convective and unsteady inertia terms may be neglected in the equations of motion. Introducing a stream function ψ and eliminating the pressure, we obtain the following differential equation for ψ:

$$\nabla^4 \psi = 0. \tag{8}$$

This linear differential equation is independent of time, i.e. this flow is also quasi-steady. We may therefore solve for the flows caused by the various external forces separately and superpose the results.

The flow corresponding to the constant shear stress τ due to the undisturbed air flow is trivial; it is just a linear velocity profile. For the wave-like disturbances we can make the following separation ansatz

$$\psi(x, y) = \phi(y)\, e^{i\alpha x}. \tag{9}$$

Substitution in (8) yields the differential equation

$$\phi'''' - 2\alpha^2\phi'' + \alpha^4\phi = 0, \tag{10}$$

which may be solved analytically since it has the four fundamental solutions

$$\sinh \alpha y; \quad \cosh \alpha y; \quad y \sinh \alpha y; \quad y \cosh \alpha y.$$

The boundary condition at the solid wall requires vanishing velocity, i.e.

$$\phi(-h) = 0, \quad \phi'(-h) = 0. \tag{11}$$

At the liquid–air interface the boundary conditions may be satisfied in the linear approximation at the undisturbed interface location $y = h$. We have

$$\left.\begin{aligned} \mu\left(\frac{\partial u}{\partial y} + \frac{\partial v}{\partial x}\right) &= \mu[\phi''(0) - \alpha^2\phi(0)]\, e^{i\alpha x} = \tau, \\ \mu\left(\frac{\partial^2 u}{\partial y^2} + \frac{\partial^2 u}{\partial x^2}\right) &= \mu[\phi'''(0) - \alpha^2\phi'(0)]\, e^{i\alpha x} = \frac{\partial p}{\partial x}, \end{aligned}\right\} \tag{12}$$

where μ is the viscosity of the liquid, τ is the shear stress determined in the air flow problem, and $\partial p/\partial x$ is the pressure gradient determined in the air flow problem plus the additional pressure gradient caused by the surface tension σ at the liquid–air interface in conjunction with the interface curvature.

We introduce the dimensionless quantities

$$h_* = \frac{h}{\delta}, \quad \sigma_* = \frac{\sigma}{\mu U_\infty}, \quad \dot{s}_* = \frac{\dot{s}\delta}{sU_F}, \tag{13}$$

where $U_F = g'(0)\, h\rho\nu U_x/(\mu\delta)$ is the undisturbed interface speed, ρ is the air density and $\dot{s} = i\alpha\phi(0)$ is the y-component of the disturbance velocity of the wave crest.

By following the procedure above, we obtain

$$\dot{s}_* = -\frac{\sigma_* \alpha_*^4 h_*^2 f_p}{3g'(0)} - \frac{h_* \alpha_*}{g'(0)}[\tfrac{1}{3}h_* B'''(0) f_p - \tfrac{1}{2}B''(0) f_\tau], \tag{14}$$

in which we have used the abbreviations

$$f_\tau = \frac{\tanh^2 z}{z^2}, \quad f_p = \frac{\tfrac{3}{2}[\tanh z(1 + z \tanh z) - z]}{z^3}, \tag{15}$$

where $z = \alpha_* h_* = \alpha h$.

The functions f_τ and f_p tend to 1 as $z \to 0$, i.e. as the ratio of film thickness to wavelength goes to zero. They provide the influence of the finite film thickness, which manifests itself in a departure of the velocity profile from the linear or parabolic form, caused by the shear stress and pressure disturbances.† We recognize further that the disturbance stream function of the air flow enters into (14) only in the form of the second and third derivatives of the imaginary part at $\eta = 0$; i.e. only those parts of the shear stress and pressure disturbances that are phase shifted relative to the surface wave by $\frac{1}{2}\pi$ enter the amplification rate. The two other, in-phase parts

† Note that, though Craik's analysis starts from the Orr–Sommerfeld equation, his subsequent assumptions reduce the problem effectively to $\Psi_{yyyy} = 0$. This corresponds to $f_\tau = f_p = 1$, which is, however, not admissible even in the case of our thinner films.

cause an increase of the surface wave speed over the material speed of the undisturbed surface (i.e. over U_F), which will not be further considered here.

We now have all the relations needed to determine the amplification or damping rate of a disturbance of given wavelength, for a given boundary layer and liquid layer.

2.4. *Simplified representation of the results*

If $\dot{s}_*$ is determined from the above relations it is obtained as a function of the following quantities:

$$\dot{s}_* = F(\alpha_*, h_*, Re, \sigma_*, g(\eta)). \tag{16}$$

By varying the wavenumber α_* one obtains the special wavenumber α_{*m} for which $\dot{s}_*$ reaches a maximum:

$$\alpha_{*m} = G(h_*, Re, \sigma_*, g(\eta)). \tag{17}$$

This is the wavenumber that should be observable in an experiment.

For large wavenumbers α_* the disturbance decays rapidly with increasing y in the air flow, i.e. the important part of the disturbance motion occurs in a thin sublayer of the boundary layer. In that case only the linear portion of the laminar-boundary-layer velocity profile is important and the quantities ν/u_τ and u_τ are likely to prove more suitable scaling parameters than δ and U_∞. (Here $u_\tau = (\tau/\rho)^{\frac{1}{2}}$ is the friction velocity.) Accordingly we introduce new dimensionless variables

$$\left.\begin{aligned} \alpha_+ &= \frac{\alpha\nu}{u_\tau} = \frac{\alpha_*}{(g'(0)\,Re)^{\frac{1}{2}}}, \quad h_+ = \frac{hu_\tau}{\nu} = h_*(g'(0)\,Re)^{\frac{1}{2}}, \\ \sigma_+ &= \frac{2\sigma}{\rho\nu u_\tau} = 2\sigma_*\left(\frac{Re}{g'(0)}\right)^{\frac{1}{2}}, \quad \dot{s}_+ = \frac{\dot{s}\nu}{su_\tau U_F} = \frac{\dot{s}_*}{(g'(0)\,Re)^{\frac{1}{2}}}. \end{aligned}\right\} \tag{18}$$

Under the circumstances assumed here, any further influence of Re and $g(\eta)$ may be expected to become negligible so that the functional forms

$$\dot{s}_+ = H(\alpha_+, h_+, \sigma_+), \quad \alpha_{+m} = I(h_+, \sigma_+) \tag{19}$$

approximately account for the variables affecting the quantities of interest.

Both for the presentation of the results and for the reduction of numerical effort the step from (17) to (19) would give considerable advantages. Whether or not it is justified has to be left to example calculations.

2.5. *Numerical computation*

For the numerical computation we consider the laminar flat-plate boundary layer. According to the arguments presented in the previous section, the results should apply approximately also to other boundary layers. To simplify the computation we replace the Blasius profile by the approximate Pohlhausen profile

$$g(\eta) = 2\eta - 2\eta^3 + \eta^4. \tag{20}$$

For a given value of α_* we then solve (4) with the boundary conditions (6) and (7). This is done by a numerical computation of one solution that satisfies the boundary conditions at $\eta = 0$ and four further, linearly independent solutions that satisfy the corresponding homogeneous boundary conditions. These may be combined linearly in such a way as to satisfy the boundary conditions at $\eta = 1$. For larger Reynolds numbers, and especially for the case of the turbulent boundary layer treated below, difficulties may arise because of precision limits. However, these can be avoided

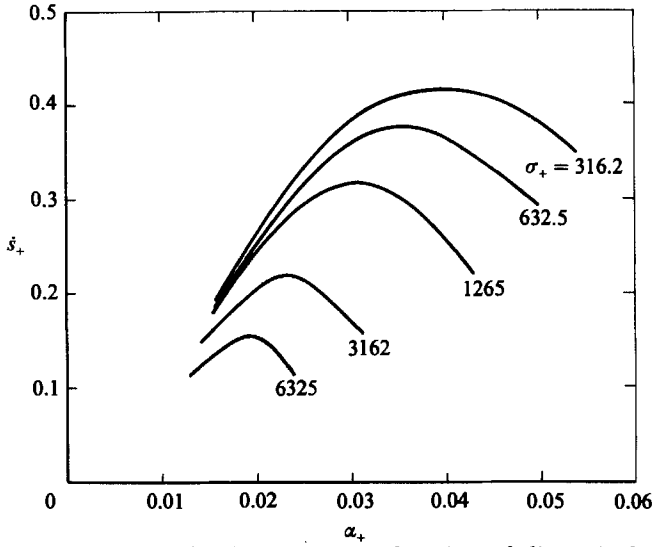

FIGURE 3. Dimensionless amplification rate as a function of dimensionless wavenumber and dimensionless surface tension. Evaluated for $Re = 2000$, $h_+ = 31.62$, laminar flat-plate boundary layer.

easily by continuing the exponential decay solution (valid at $\eta > 1$) to values of $\eta < 1$ with the aid of the inviscid equations and matching it at a point below $\eta = 1$.

This calculation yields the quantities $B''(0)$ and $B'''(0)$ necessary for the determination of the amplification rate $\dot{s}_*$ from (14).

Starting with a given boundary layer and liquid layer (i.e. fixed $g(\eta), Re, h_*, \sigma_*$) and varying α_*, one obtains $\dot{s}_*$ as a function of α_*, a curve with a pronounced maximum in the region of positive values of $\dot{s}_*$. Computations of this kind were performed for a Pohlhausen flat-plate profile at $Re = U_\infty \delta/\nu = 2000$ for a range of values of h_* and σ_* and transformed into the variables α_+, h_+ and σ_+ for the reasons given in §2.4. Examples of the resulting curves are plotted in figure 3. From such curves the $\alpha_{+\mathrm{m}}$ values, i.e. the values at which $\dot{s}_+$ reaches a maximum, may be determined. They are plotted against σ_+ for various values of h_+ in figure 4. The wavelength of the most strongly amplified disturbance may be obtained directly from this graph for a given liquid layer and a given boundary layer.

In addition, one of these curves has been recalculated for $Re = 1000$ at otherwise equal conditions. This curve is also plotted in figure 4. It shows that the (additional) influence of Re is indeed small, as assumed. The range $1000 < Re < 2000$ covers the range of interest below transition.

2.6. *Turbulent boundary layer*

The results of the previous sections for laminar boundary layers show that, especially for small wavelengths, the flow disturbance is restricted mainly to the near-wall region of the boundary layer, where the velocity profile is linear. In a turbulent boundary layer there also exists a thin viscous sublayer in which momentum exchange occurs only owing to the molecular viscosity of the air and not through turbulent mixing. For sufficiently small wavelengths which cause disturbance flows that decay over the viscous sublayer thickness, the same relations must therefore apply as for the laminar boundary layer, if the dimensionless quantities of §2.4 are used.

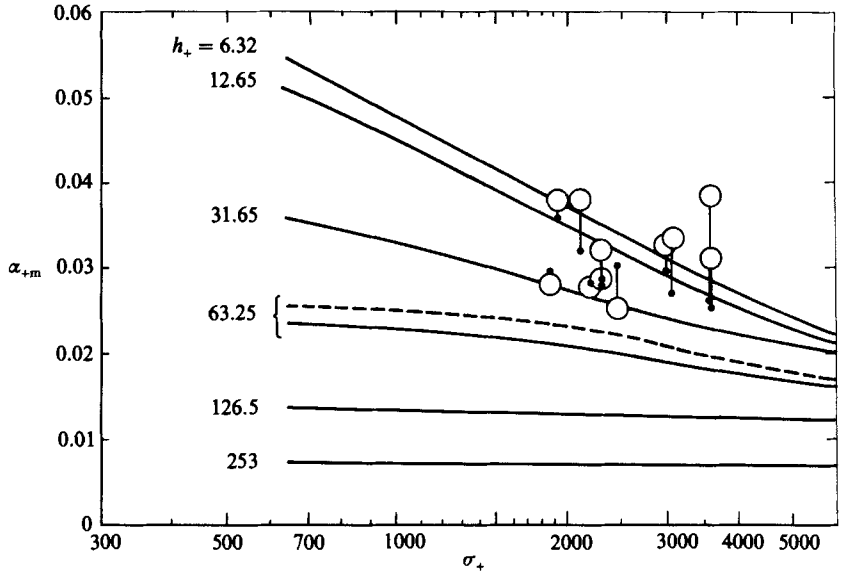

FIGURE 4. Most strongly amplified wavenumber with a laminar flat-plate boundary layer. Experimental results are shown as circles. The points attached to the circles by lines indicate the positions where the circles should be for agreement with the theory according to the value of h_+ determined from experiment. ——, $Re = 2000$; – – –, $Re = 1000$.

A considerably better approximation, valid up to larger wavelengths, is obtained by computing the flow as in the laminar case, but with an empirical boundary-layer mean velocity profile. Since only the near-wall region is of interest, it is appropriate to use the universal law of the wall. This neglects the effect of the Reynolds stress on the disturbance flow, but retains to first order the correct influence of the main flow velocity on the disturbance pressure.

The physical reason for the fact that this approach yields a considerably better approximation is that in the disturbance motion, just as in laminar stability theory, there exists a near-wall layer in which viscous forces are important, while they may be neglected elsewhere. Our approximation should therefore be valid as long as this sublayer is thinner than the viscous sublayer. The formation of the 'disturbance sublayer' is more easily understood by observing that the waviness of the wall generates a pressure that fluctuates in the x-direction and whose amplitude is largest at the wall. However, it is just at the wall where longitudinal motions are brought to rest by viscous forces.

Figure 5 shows the so-computed dimensionless wavenumber of maximum amplification rate, α_{+m} plotted against σ_+ for various values of h_+. It may be seen that much smaller wavenumbers result than in the case of the laminar boundary layer.

Of course, the calculation could be improved further by introducing an eddy viscosity, but the results would then depend on somewhat arbitrary assumptions about the eddy viscosity.

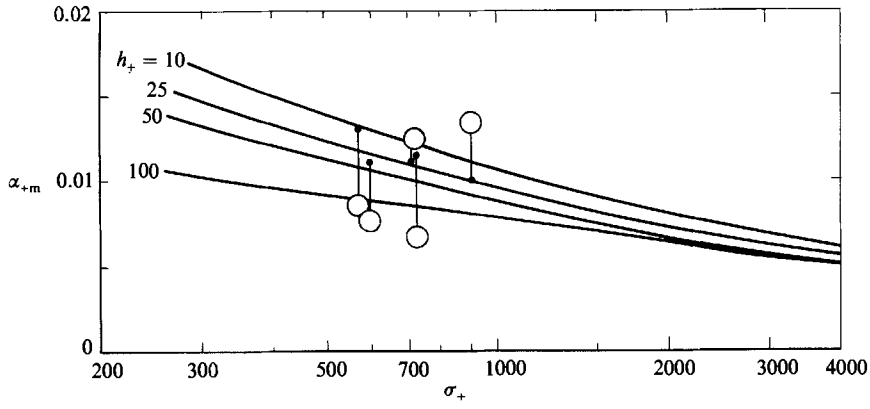

FIGURE 5. Most strongly amplified wavenumber with a turbulent boundary layer. For notation of experimental symbols see caption of figure 4.

3. Experiment

3.1. *Design of the experiment, experimental set-up and technique*

In order to examine the occurrence and features of surface waves in an experiment, it is necessary to be able to start the flow in a time that is sufficiently short compared with the establishment time of the waves. Since the high-speed wind tunnel HKG at the DFVLR-AVA Göttingen, a 'suck-down' facility operating between the atmosphere and a large vacuum tank, is started with a fast valve downstream of the test section, it is ideal for our purpose. Normally this facility is operated in the Mach-number range $0.4 < M < 2.5$ and the range of present interest is $0 < M < 0.25$. For this reason wooden blocks were added to the jaws of the adjustable sonic throat which is located between the test section and the valve, so that the desired low speed could easily be regulated to conditions that remained constant over a test period of approximately 45 s.

For subsonic operation the tunnel has an open test section 75 cm × 75 cm in cross-section within a large tank sealing it from the laboratory. Within the test section a flat plate made of aluminium was mounted on a sting fixed to the trailing edge of the plate and mounted on the remotely adjustable incidence gear. The plate's streamwise extent is 50 cm and its width 40 cm. Normally a flat plate at zero incidence in subsonic flow should have a slender rounded leading edge to avoid leading-edge separation, transition or other disturbances. In our case it was necessary to cover the plate with the viscous liquid (oil) and to let this come to rest over some time so that it reached a uniform thickness. Hence, it seemed desirable for the plate to have a horizontal top surface and, therefore, an asymmetrical sharpened leading edge. Leading-edge separation could then be avoided by quickly giving the plate a suitable degree of negative incidence just before the flow was started. While this alters the state of the boundary layer from that of a zero-incidence layer, the incidence needed was only 10° and the effect is slight.

In order to visualize surface disturbances of small amplitude, the following technique was used. A vertical wall parallel to the tunnel axis was rigged up along the edge of the open-jet test section, with a white surface facing the flow. On this white surface, 2.5 cm broad strips of dark adhesive tape were attached at a spacing of about 5 cm, so that a coarse pattern of alternating dark and white stripes resulted.

On the other side of the open jet (opposite the wall with the striped pattern) a camera was rigged up to photograph the reflection of the pattern in the smooth oil surface acting as a mirror. As soon as the surface becomes disturbed, the reflection becomes disturbed, and this becomes visible in the picture. Of course, the method is the more sensitive the larger is the distance between pattern and mirror, and it is also most sensitive along the dark-white edges of the image in the surface. Some adjustments were necessary to optimize these parameters. It turns out that at the conditions of our experiment, it is better to focus the camera on the surface rather than on the stripe pattern, though the stripe pattern is still resolved quite well.

The camera was set to take pictures at a fixed rate up to two frames per s during each run and the plate was illuminated with an electronic flash synchronized with the shutter. An example of the results is presented in figure 6 showing a sequence of photographs from tunnel start to conditions during the run with well-established wave patterns for a flow speed of 36 m/s. These will be discussed in more detail in the next section.

The procedure of the experiment was as follows. The plate was first adjusted to the horizontal. A measured quantity of oil was poured onto the plate and allowed to spread. The sharp edges of the plate prevented any spilling. The film thickness was measured at various points with a micrometer. A typical value of the film thickness was 0.15 mm. While the average thickness was well controllable by measuring the volume of oil, the spatial variation before the shot was as much as $\pm 10\%$. The tunnel was then closed, and the incidence adjusted. Immediately thereafter the camera and tunnel were started. The time between incidence adjustment and tunnel start was approximately 1 s. No motion of the liquid film under gravity could be detected in the photographs during this time. The surface tension of the oil, measured by a capillary technique, was 0.02 N/m and its viscosity was 2.9 g/(cm s).

In order to evaluate the results, a centimeter grid was placed on the plate and photographed with the plate and camera in the same condition as during the run. Overlaying this on the photographs facilitates the measurement of the wavenumber of the observed waves because it deconvolutes the perspective distortion by providing an equally distorted grid.

3.2. *Experimental results*

In this section we present the experimental results in the form of the photographs obtained, and briefly discuss their qualitative features. The quantitative evaluation and comparison with theory is left to §4.

The first example, with a laminar air boundary layer has already been introduced with the sequence of 5 photographs of figure 6 at a free-stream speed of 36 m/s. The first frame shown, (figure 6*a*), is taken just after tunnel start. The second frame shown (figure 6*b*), taken 10 s after tunnel start shows two interesting features. First, oblique waves appear near the leading edge which show great regularity and occur at an angle very close to 45° from the flow direction. These, in fact, already appear on the first frame, taken less than a second after tunnel start. Secondly, the beginnings of waves of a larger wavelength appear at the edges of the images of the dark stripes further downstream. The third frame shown (figure 6*c*), was taken at 14 s after tunnel start and shows that the second group of waves has been amplified further while the oblique waves have remained of much the same amplitude. The fourth and fifth frames (figures 6*d* and 6*e*), taken at 18 and 24 s show a continuation of this trend.

The second group of waves, which appear later and are amplified more strongly,

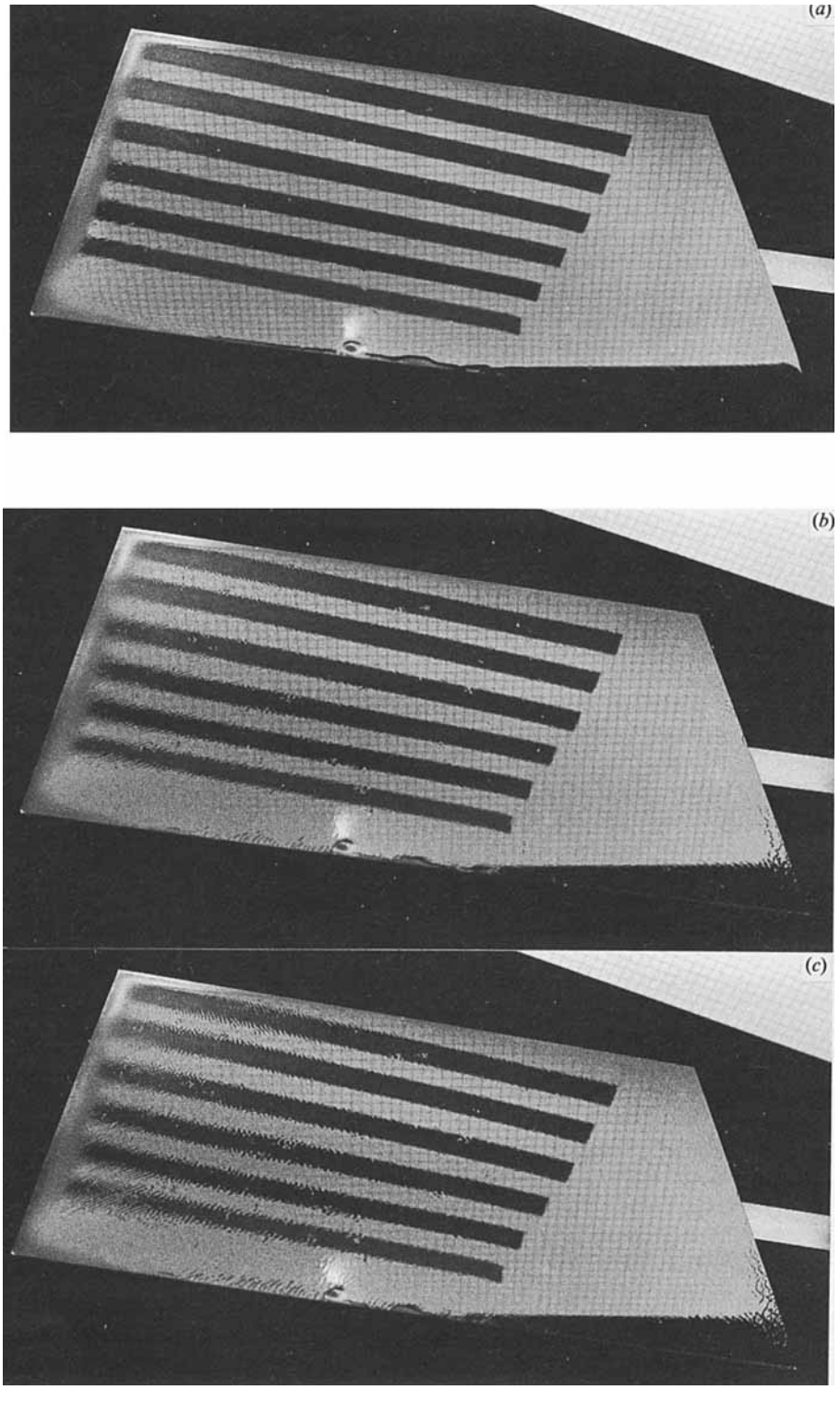

FIGURE 6(a–c). For caption see facing page.

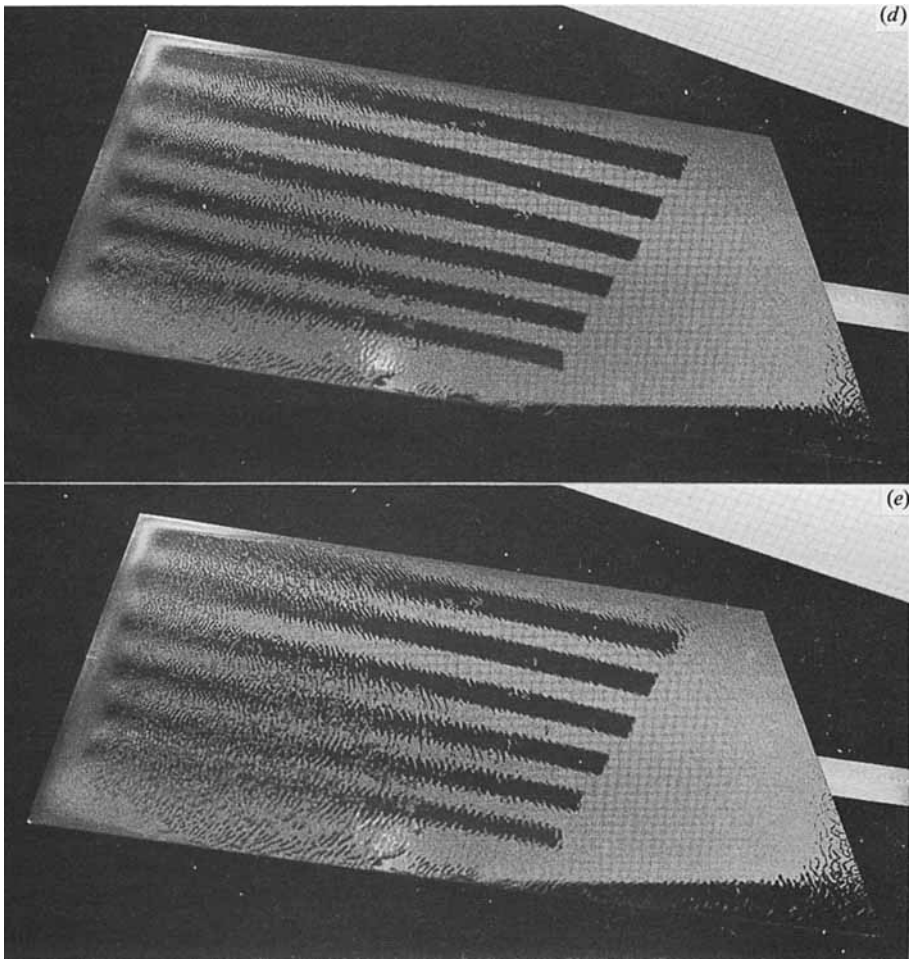

FIGURE 6. Photographs of the surface during the run at $U_\infty = 36$ m/s. Flow from left to right. the plate is shown in perspective distortion. It is covered with oil and reflects a pattern of broad strips of dark adhesive tape on a vertical wall behind the flow to amplify the visualization of surface waves. A rectangular grid inscribed on the wall is also seen in the reflection. (*a*) Just after tunnel start. (*b*) 10 s after tunnel start. Note oblique waves near the leading edge and beginnings of transverse waves at the edges of the images of the dark strips on the left half of the plate. (*c*) 14 s after tunnel start. Transverse waves have grown in amplitude. (*d*) 18 s and (*e*) 24 s after tunnel start. Note continued amplification of transverse waves.

occur virtually in a transverse direction to the flow. These we interpret to be the waves predicted by the theory. Interpretations of the other group, the oblique regular waves appearing earlier and not being amplified as strongly, can only be speculative.

As a second example we show in figure 7 a single frame taken 2 s after tunnel start at a flow speed of 69 m/s, at which the boundary layer is laminar near the leading edge, turbulent near the trailing edge, and transitional over most of the length. This may easily be recognized by the long turbulent wedges, between which, i.e. in the laminar portions, the features of figure 6 are generally repeated on a smaller wavelength scale. Also, the waves in the turbulent portions, both within the turbulent wedges and where these have grown together downstream, have quite

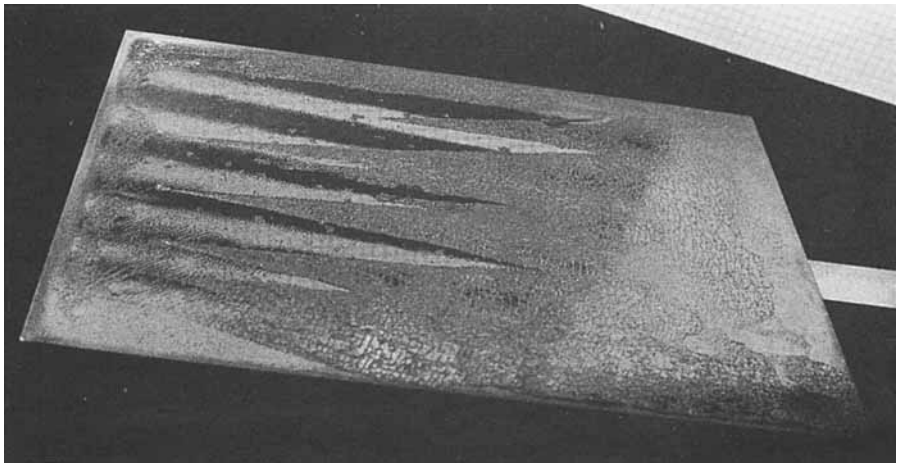

FIGURE 7. Flow speed = 69 m/s, 2 s after tunnel start. Transitional flow. Note turbulence wedges and laminar flow behaviour between them. Also note turbulent behaviour far downstream where wedges have joined.

different features. They are obviously far from being sinusoidal in shape, though a reasonably regular wavelength may be observed.

At a slightly higher speed, 84 m/s, figures 8(*a*) and 8(*b*) show two frames taken at 7 and 15 s respectively. These display clearly, that near the front an accumulation of material and a formation of longitudinal stripes has taken place. However, further downstream the typical transverse waves of turbulent flow still portray a fairly regular pattern.

4. Comparison between theory and experiment, and discussion

Measurements of the wavenumber of the observed waves were made at points where the waves are particularly clearly seen at different times and positions on the plate in the photographs obtained in 15 runs. These were then converted to the dimensionless variables α_+, σ_+ and h_+ by using the wall shear stress according to the correlations with theoretical flat-plate laminar boundary layer or the flat-plate turbulent boundary layer, for laminar and turbulent flow respectively.

The resulting values are plotted in figures 4 and 5 in order to compare them with the theory. In order to relate the measured points, drawn as circles, to the appropriate dimensionless layer thickness h_+ as obtained from measurements before the run, each circle is provided with a line and a point, the point being placed at the position where the circle would have to be for perfect agreement with the theory.

Large uncertainties may be expected in the measurement of the dimensional wavelength ($\pm 12\%$), in the dimensional initial film thickness ($\pm 20\%$), in the viscosity ($\pm 3\%$) and surface tension ($\pm 10\%$) of the oil, as well as in the assumption about flat-plate flow. If all of these are lumped together in an effective uncertainty in α_+ an expected uncertainty of $\pm 25\%$ results. With the exception of one point, the laminar flow results lie within the margin.

The discrepancies are much larger in the case of the turbulent boundary layer. This is not unexpected, since the assumptions of the theory are relatively crude, the waves

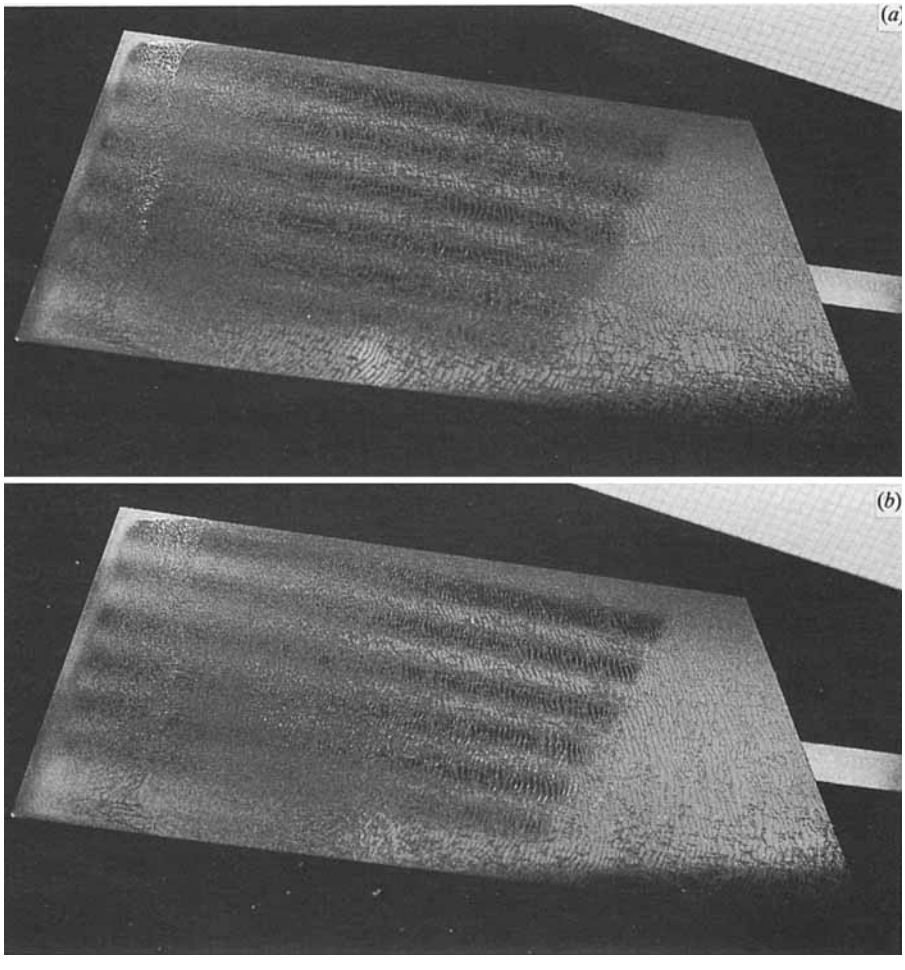

FIGURE 8. Flow speed = 84 m/s. (*a*) 7 s, (*b*) 15 s after tunnel start. Note accumulation of material near leading edge, longitudinal structure developing thereafter and transverse waves of turbulent flow further downstream.

are certainly neither sinusoidal nor of small amplitude, and the film thickness has probably been significantly increased over that prevailing before the run.

From this comparison we regard the theory as providing a quantitative description of the instability of a liquid film under a laminar boundary layer, and at least a qualitative one for the case of a turbulent boundary layer.

Comparing figure 4 with figure 5 it may be seen that for given h_+ and σ_+ the theory gives considerably higher values of $\alpha_{+\mathrm{m}}$ for laminar than for turbulent boundary layers. This is also confirmed by the experiments. The transition from laminar to turbulent boundary-layer flow, which occurs fairly sharply with change of the flow parameters, also brings with it a fairly sharp change of u_τ. Hence, the parameters h_+, σ_+ and $\alpha_{+\mathrm{m}}$ also change quite suddenly at transition. The nature of these changes is such that transition causes a significant reduction of the wavenumber α, as is also confirmed by the experiments.

The formation of transverse waves is only the first stage of the formation of the lines seen in the method of surface oil flow visualization. From observations and

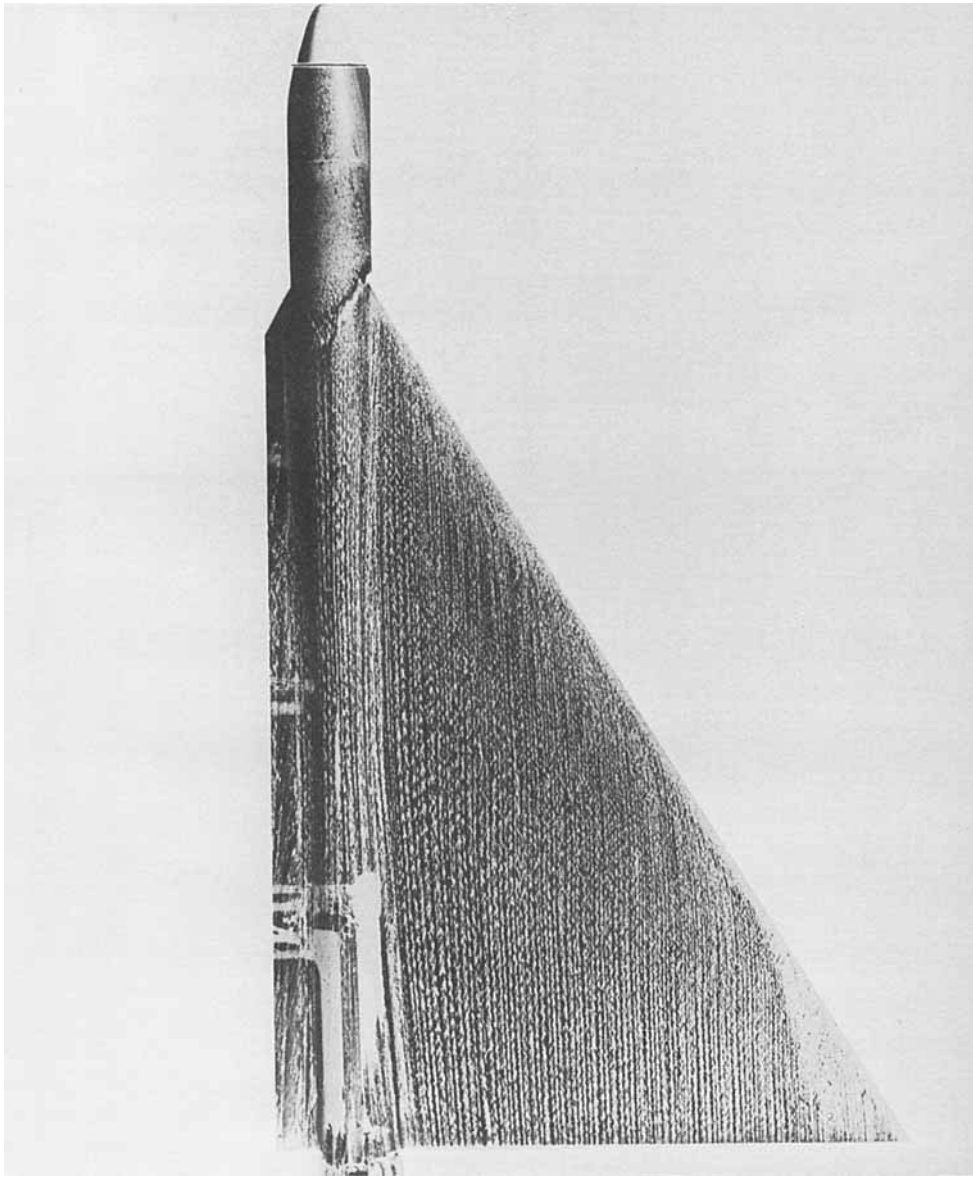

FIGURE 9. Surface oil flow visualization photograph on the pressure side of a delta wing at a free-stream Mach number of 1.22 and 7° incidence. Note the transverse oblique fine structure within the coarser regular streamwise lines.

conjecture it is expected that in a later stage the wave crests themselves display a transverse instability governed by surface tension, similar to the well-known instability of a cylinder of liquid at rest under the influence of surface tension. Evidently the pressure forces of the boundary-layer flow amplify this effect. At a later stage this leads to the formation of drops. The drops then move faster than surrounding liquid and thus clear paths that remain visible as the observed lines.

The linear theory is not able to describe these effects, of course. However, it does show that no single length governs the observed wavelength, each of h, ν/u_τ and

σ/τ taking a dominant role in different regimes. It must be expected, therefore, that the line spacing, which may be assumed to be governed essentially by the wavelength, will likewise not be controlled by any single one of these characteristic lengths.

It is possible that the regular transverse structures sometimes observed in compressible-flow visualization as a finer structure superimposed on a longitudinal line structure are a residue of the original transverse waves, see figure 9. The observed longitudinal length parameter should then coincide with the wavelength discussed before. However, though this can be explained by a physical argument, it has so far not been substantiated experimentally or theoretically.

REFERENCES

CRAIK, A. D. D. 1966 *J. Fluid Mech.* **26**, 369–392.

HORNUNG, H. 1985 In *Ernst-Becker-Gedächtnis-Kolloquium, TH Darmstadt, THD Schriftenreihe Wiss. und Technik*, vol. 28.

SQUIRE, H. B. 1953 *Br. J. App. Phys.* **4**, 167–169.

SQUIRE, L. C. 1961 *J. Fluid Mech.* **11**, 161–179.